catalysts

MDPI

Article

Effects of Different Reductive Agents on Zn-Promoted Iron Oxide Phases in the CO_2–Fischer–Tropsch to Linear α-Olefins

Yueshen Pan [1], Xiaoxu Ding [1], Chao Zhang [2], Minghui Zhu [1], Zixu Yang [1,*] and Yi-Fan Han [1,3,*]

[1] State Key Laboratory of Chemical Engineering, School of Chemical Engineering, East China University of Science and Technology, Shanghai 200237, China
[2] Institute of (Bio)pharmaceutical Research, Institute of Zhejiang University, Quzhou 324000, China
[3] Engineering Research Center of Advanced Functional Material Manufacturing, Ministry of Education, Zhengzhou University, Zhengzhou 450001, China
* Correspondence: zixu.yang@ecust.edu.cn (Z.Y.); yifanhan@ecust.edu.cn (Y.-F.H.)

Abstract: The pretreatment atmosphere has a significant impact on the performance of iron-based catalysts in carbon dioxide (CO_2) hydrogenation. In this study, we investigated the effects of carbon monoxide (CO), syngas (H_2/CO), and hydrogen (H_2) on the performance of iron-based catalysts during the pretreatment process. To evaluate the structural changes in catalysts after activation and reaction, we analyzed their morphology and particle size, the surface and bulk phase composition, carbon deposition, the desorption of linear α-olefins and reaction intermediates using transmission electron microscope (TEM), Raman spectroscopy, X-ray photoelectron spectroscopy (XPS), X-ray diffraction (XRD), Mössbauer spectroscopy (MES), temperature-programmed desorption (TPD), and in situ diffuse reflectance infrared Fourier transform spectroscopy (in situ DRIFTS). Raman and XPS showed that the H_2 pretreatment catalyst caused the absence of iron carbides due to the lack of carbon source, and the CO and syngas pretreatment catalysts promoted the formation of carbon deposits and iron carbides. While the bulk phase of the CO and syngas pretreatment catalyst mainly consists of iron carbide (FeC_x), XRD and MES revealed that the bulk phase of the H_2 pretreatment catalyst primarily consisted of metallic iron (Fe) and iron oxide (FeO_x). The composition of the phase is closely associated with its performance at the initial stage of the reaction. The formation of olefins and C_{5+} products is more encouraged by CO pretreatment catalysts than by H_2 and syngas pretreatment catalysts, according to in situ DRIFTS evidence. Ethylene (C_2H_4)/propylene (C_3H_6)-TPD indicates that the CO pretreatment catalyst is more favorable for the desorption of olefins which improves the olefins selectivity. Based on the analysis of the TEM images, H_2 pretreatment stimulated particle agglomeration and sintering. In conclusion, the results show that the CO-pretreatment catalyst has higher activity due to the inclusion of more FeO_X and Fe_3C. In particular, the presence of Fe_3C was found to be more favorable for the formation of olefins and C_{5+} hydrocarbons. Furthermore, carbon deposition was relatively mild and more conducive to maintaining the balance of FeO_x/FeC_x on the catalyst surface.

Keywords: CO_2 hydrogenation; iron carbides; reductive agents; α-olefins

check for updates

Citation: Pan, Y.; Ding, X.; Zhang, C.; Zhu, M.; Yang, Z.; Han, Y.-F. Effects of Different Reductive Agents on Zn-Promoted Iron Oxide Phases in the CO_2–Fischer–Tropsch to Linear α-Olefins. *Catalysts* **2023**, *13*, 594. https://doi.org/10.3390/catal13030594

Academic Editor: Zhong-Wen Liu

Received: 20 February 2023
Revised: 8 March 2023
Accepted: 13 March 2023
Published: 16 March 2023

1. Introduction

The consumption of fossil fuels and human activities have accelerated CO_2 emissions, which may lead to a number of issues, such as global warming and ocean acidification [1,2]. A feasible strategy to mitigate this issue is CO_2 hydrogenation to value-added chemicals, such as methanol, olefins and aromatics, or liquid fuels using green hydrogen [3–5]. Methanation of CO_2 and the reverse water gas shift into CO are two techniques by which CO_2 is converted into various chemicals [6], while CH_4 and CO are regarded as the CO_2RR species with the highest commercial value [7]. Olefin synthesis from CO_2 mainly occurs via two different routes, namely the methanol-mediated route and the CO_2 Fischer–Tropsch (CO_2-FT) synthesis route. The former process occurs at temperatures at approximately 400 °C, which results in a very low olefin yield due to high CO selectivity (>50%). CO_2-FT is a multi-step process that combines reverse water gas shift (RWGS) and FTS. CO_2 is initially converted to CO by the RWGS reaction and subsequent hydrogenation of CO to olefins via the FTS reaction [8,9]. CO, which is generated by RWGS, is an important intermediate of the CO_2-FT reaction, while competing CO_2 methanation hinders the progress of RWGS reaction and reduces the CO yield [10]. The RWGS reaction mainly contains two pathways, which are redox and association pathways [11]. Under reaction conditions, the materials containing reducible oxides mostly follow the redox pathway [12], while the association pathways are mainly dominated by noble metal nanoparticles (NPs) on reducible support catalysts [13]. This indicates that the RWGS reaction is highly dependent on the type of catalyst and on reaction conditions [14]. Iron-based catalysts have emerged as the ideal candidates for CO_2-FT because they have shown exceptional activity for both reaction steps. Typically, the active phase of RWGS, which converts CO_2 to CO, is considered to be Fe_3O_4 [5,15], and iron carbides are regarded as active phases in Fischer–Tropsch synthesis reactions [16,17].

$$CO_2 + H_2 \xrightarrow{RWGS} CO + H_2O$$

$$nCO + 2nH_2 \xrightarrow{FTS} -(CH_2)_n- + H_2O$$

Under reaction conditions, catalyst precursors, which are normally in the form of bulk iron oxides, are reduced and carburized to form active iron carbides for C–C coupling. The carbides can also be re-oxidized by water and CO_2 during the reaction. The transformation of iron precursors to iron carbides is recognized as a complex and dynamic process that involves oxygen removal, carbon diffusion, hydrogenation and surface carbon deposition. The structure and composition of the catalyst strongly depends on the catalyst preparation methods, promoters, pretreatment protocols and reaction conditions.

Pretreatment conditions, in particular the composition of pretreatment gas, have been reported to strongly affect the structure and catalytic performance of the iron-based FT catalysts. Bukur et al. studied the effects of different pretreatment atmospheres on iron-based catalysts and found that CO and syngas pretreatment catalysts were more susceptible to deactivation than hydrogen pretreated catalysts, but were more conducive to the formation of long-chain hydrocarbons [18–20]. However, Lee et al. argued that CO-pretreated catalysts contained more iron carbides, which improved the FTS activity and olefin selectivity [21]. In another study by Li et al., the authors reported a selectivity shift to heavy hydrocarbons upon increasing CO partial pressure in the pretreatment H_2/CO gas mixture [22]. In the field of electrocatalysis, Bhalothia et al. processed catalysts under different reduction conditions, obtained catalysts with the same composition but different nanostructures, and clarified their structure-dependent ORR performance [23].

The dynamic transformation of iron-based FT catalysts during activation was studied experimentally using in-situ characterization techniques and theoretically using atomistic thermodynamics. Using in-situ X-ray diffraction, Lu et al. tracked the temperature-dependent evolution of Fe_3O_4, FeO, Fe (0), Fe_5C_2 and Fe_3C under the syngas environment with varying H_2/CO ratios. They further obtained a high-purity (95%) χ-Fe_5C_2 catalyst under the optimal H_2/CO ratio of two. The obtained catalyst showed enhanced FT activity and the selectivity of C_{5+} hydrocarbons [24]. Emiel de Smit et al. correlated the stability and reactivity of various iron carbides (e.g., ε-Fe_2C, χ-Fe_5C_2, and θ-Fe_3C) with carbon chemical potential (μ_c) and reaction temperature. Different gas phase compositions, which have different carbon chemical potentials, and reaction temperature have an impact on the relative thermodynamic stability of iron carbides, thereby regulating the type of iron carbides formed. In particular, high μ_c is beneficial to the formation of χ-Fe_5C_2, and low μ_c is conducive to the formation of θ-Fe_3C. High μ_c at low temperature favors the formation of ε-Fe_2C. Under FTS conditions, the catalysts with crystalline χ-Fe_5C_2 as their major component were quite sensitive to oxidation, whereas those with θ-Fe_3C and amorphous carbide phases exhibited decreased activity and selectivity, primarily due to the accumulation of carbonaceous deposits on the catalyst surface, indicating that the final catalyst performance was significantly influenced by the amorphous phases and the resulting textural properties [25]. A recent study conducted by Li et al., pointed that the carbonization rate and the equilibrium phase composition iron catalyst is not solely determined by the theoretical μ_C of the pretreatment gas, but also related to kinetic and entropic variables [26]. Although prominent endeavors have been devoted to study the influence of pretreatment conditions on the chemical composition, structure, and the resulting performance of catalysts, the pretreatment methods to deliver preferential iron phases remain elusive and controversial.

The dynamic evolution of iron catalysts in the FTS reaction was also observed in CO_2 hydrogenation conditions. Han et al. used operando XRD/Raman to study the phase transition of bulk iron-based catalysts in direct CO_2-FT to olefins, and believed that the oxidation of iron carbides was the main reason for the iron catalyst deactivation. The activity and C_2–C_4 olefins selectivity of the catalyst can be greatly restored by CO_2-CO regeneration treatment. Additionally, various iron-based precursors will produce several different iron carbides. While θ-Fe_3C obtained from γ-Fe_2O_3 is more desirable for the formation of C_{5+} hydrocarbons, χ-Fe_5C_2 derived from α-Fe_2O_3 is favorable for the generation of lower olefins [27,28]. Recently, Guo's team combined experiments and theoretical calculations to reveal the relationship between the dynamic structure and catalytic performance of iron-based catalysts during CO_2 hydrogenation. The results showed that the change of surface composition depends on the balance of oxidation and carbonization and it is highly sensitive to the operating conditions (e.g., GHSV and H/C), where by-product water is critical [29]. Andrey S. Skrypnik et al. studied the role of different iron species in CO_2 hydrogenation, and found that the proportion of iron carbides was positively correlated with the selectivity of C_{2+} hydrocarbons. Fe_3O_4 and metallic Fe are responsible for CO hydrogenation to CH_4; however, the main function of Fe_3O_4 is to promote CO_2 conversion into CO through the RWGS reaction [30].

To improve the olefins selectivity and simultaneously suppress the formation of undesired CO and methane, iron catalysts must be promoted with alkali metals and transition metals, such as Zn, Cu, and Mn [31–33]. These metals, mainly in their oxide form, can function as an electronic or structural promoter, enhancing the reducibility of the iron oxide precursor, dispersion and stability of resulting iron carbides, and surface basicity. In a previous work, the Fe_2Zn_1 catalyst achieved the selectivity of C_2–C_7 olefins in the gas phase product of 57.8% and C_{4+} olefins selectivity in the liquid phase product of 81.9% when the CO_2 conversion was 35%. The catalyst enables RWGS to occur on the formed ZnO and highly dispersed FeO_X, and C–C coupling and olefin formation on FeC_x. The aggregation and interaction of Na and Fe to the catalyst surface during activation inhibits the oxidation of FeC_x, resulting in excellent stability [34]. In addition, the introduction of Zn promoted CO_2 conversion, olefin desorption and chain growth, and inhibited the secondary hydrogenation of olefins, while changing the balanced ratios of FeC_x/FeO_x during the reaction [31].

It is challenging to explore the CO_2-FT process due to the intricacy of the phase and structural transitions involved in iron-based catalysts and the limitations of characterization techniques. Among them, the effects of the pretreatment atmosphere on iron-based catalysts in the CO_2-FT procedure has thus received little consideration. In addition, in situ DRIFTS is a very infrequently used technique within high pressure reactions, despite being a crucial tool for identifying species adsorbed on catalyst surfaces. In this study, we investigated the impacts of pretreating protocols on the phase composition of a Fe-Zn-Na catalyst prepared via a coprecipitation method, and pretreated the catalyst using different activation agents, namely 10% CO, 5% CO/5% H_2 and 10% H_2. The chemical composition and structure of the catalysts after reductive pretreatment and CO_2-FT reaction were investigated using multiple characterizations. Meanwhile, the possible adsorbed species on catalyst, pretreated under different conditions were investigated using high-pressure diffuse reflectance FTIR spectroscopy (DRIFTS). A direct correlation between the reductive pretreatment and the mechanistic pathways were discussed.

2. Results and Discussion

2.1. Catalytic Performance of CO_2 Hydrogenation

The CO_2 conversion and the selectivity of CO, CH_4, C_2–C_4 alkenes and alkanes and C_{5+} products in the CO_2 hydrogenation of catalysts pretreated with different reductive gases are shown in Figures 1a and S1a,b. The hydrocarbon distribution of the liquid products is displayed in Figures 1b and S1c,d.

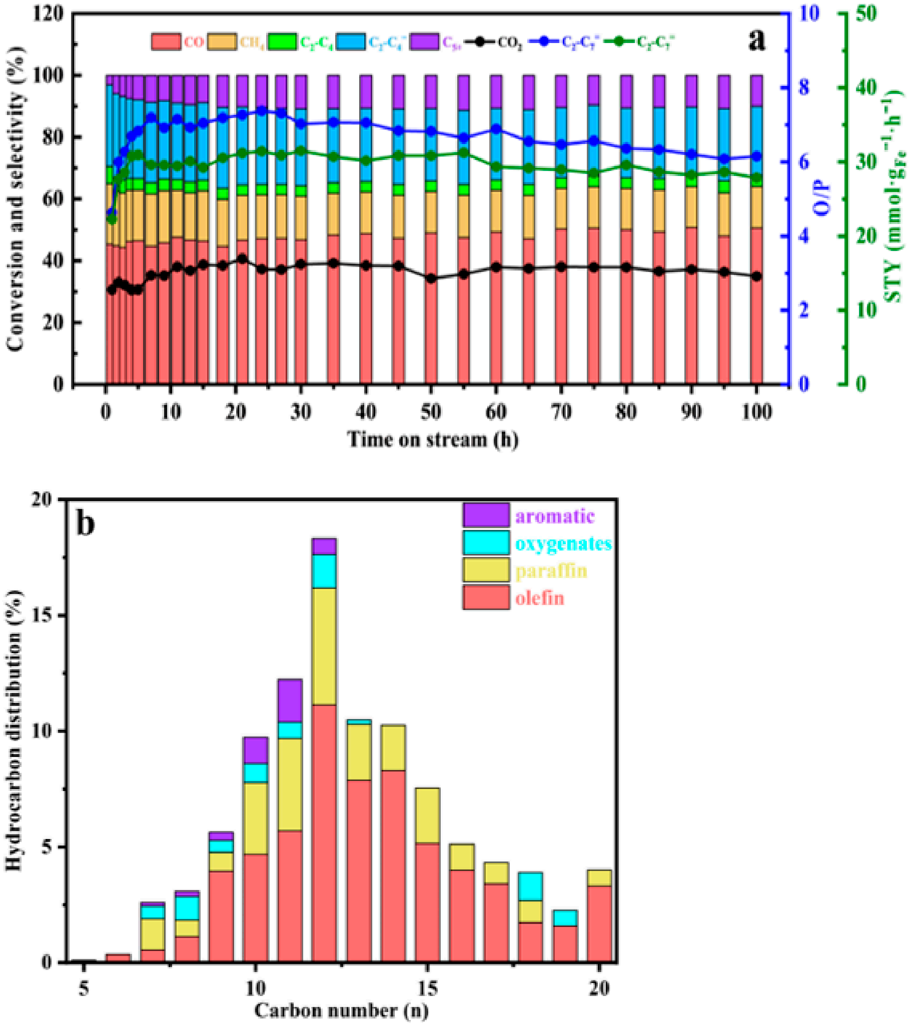

Figure 1. (**a**) 100 h time on stream and (**b**) liquid product analysis of the Fe_2Zn_1 activated by 10% CO/Ar under reaction conditions (330 °C, 1.5 MPa, 60,000 mL·g^{-1}·h^{-1}).

The pretreatment gases showed different impacts on the performance of CO_2 hydrogenation. First of all, the performance of the catalysts pretreated by different atmospheres did not show obvious deactivation within 100 h, indicating that the catalyst materials pretreated with different reductive gases remained stable during the CO_2-FT reaction. Interestingly, the induction period, i.e., the time needed to establish a stable conversion and product composition, of the catalyst subjected to different pretreatment gases were distinct. For instance, the CO and syngas pretreated catalyst showed a sharp increase in the olefin/paraffin (O/P) ratio within 10 h TOS and subsequently stabilized at 20 h. In contrast, the H_2 pretreated catalyst showed a dramatic decrease in the O/P ratio within 50 h TOS.

When comparing the stabilization period data (100 h) of different atmospheres' pretreatment catalysts, it can be observed that the CO_2 conversion of the H_2 pretreatment catalyst was approximately 28%, while the CO and syngas pretreatment catalysts were 35% and 32%, respectively. As for product selectivity, the H_2-pretreated catalyst formed substantial amounts of C1 products (CO: 61.1%, CH_4: 13.2%) and small amounts of C_2–C_4 olefins (15.9%) and C_{5+} (6.7%). The lowest CO selectivity (50.6%) and highest selectivity of C_2–C_4 olefins and C_{5+} products (22.3% and 10%) were obtained in CO pretreated catalysts. The product distribution of the syngas pretreated catalyst was in between, where the selectivity of C_2–C_4 olefins and C_{5+} products were 18.9% and 7.9%, respectively, while the CO selectivity was 55.6%. The selectivity of CH_4 and C_2–C_4 alkanes was not significantly impacted by the pretreatment gases; CH_4 had a selectivity of roughly 13%, while C_2–C_4 alkanes had a selectivity of approximately 3%. For the STY of C_2-C_7 olefins, the catalysts of different atmospheres' pretreatment increased over time, and finally remained stable. Among them, the initial STY of the CO pretreatment catalyst was the highest (22 $mmol \cdot g_{Fe}{}^{-1} \cdot h^{-1}$), while that of syngas and H_2 pretreatment was similar (12 $mmol \cdot g_{Fe}{}^{-1} \cdot h^{-1}$ and 14 $mmol \cdot g_{Fe}{}^{-1} \cdot h^{-1}$). The final CO pretreatment catalyst was stable at 28 $mmol \cdot g_{Fe}{}^{-1} \cdot h^{-1}$, while that of syngas and H_2 was 24 $mmol \cdot g_{Fe}{}^{-1} \cdot h^{-1}$ and 21 $mmol \cdot g_{Fe}{}^{-1} \cdot h^{-1}$, respectively. The highest O/P of 6.2 was obtained in the CO pretreated catalyst. Both syngas and H_2 pretreatment catalysts possess an O/P of 5.1. The O/P of the products in the liquid phase were 2.47 (for CO pretreatment), 2.36 (for syngas pretreatment), and 2.02 (for H_2 pretreatment). In short, CO pretreatment catalysts displayed better activity and olefin selectivity compared to H_2 and syngas pretreatment catalysts, favoring the production of C_2–C_4 olefins and C_{5+} hydrocarbons.

2.2. Structure and Properties of Fresh Catalysts

The elemental composition of the fresh catalyst was 44% for Fe, 25% for Zn and 1.5% for Na measured by ICP.

The XRD pattern of the fresh catalyst is shown in Figure S2a. The characteristic peaks located at 29.9° and 35.3° were attributed to the spinel $ZnFe_2O_4$ (JCPDS 89-1012). The Raman spectra (Figure S2b) of fresh catalysts were in agreement with the XRD. The typical peaks of Raman shift 451 cm^{-1} and 647 cm^{-1} were attributed to $ZnFe_2O_4$, suggesting that the catalyst includes only $ZnFe_2O_4$. The morphology and particle size of the catalyst were investigated by TEM (Figure S2c). The particle size of the fresh catalyst was 7.9 ± 0.1 nm.

2.3. Structure and Properties of Pretreated Catalysts

To illustrate the effect of different activation atmospheres on the reduction and carbonization processes of the catalysts, we characterized the pretreated and spent catalysts.

The surface phases of the activated catalysts were characterized by Raman and XPS. As shown in Figure S3, all three activated catalysts showed the Fe-O vibrational peaks at the Raman shift of 660 cm^{-1}, whereas the CO and syngas activated catalysts showed the distinctive peaks of carbon deposition at the Raman shift of 1350 cm^{-1} and 1590 cm^{-1}, which were ascribed to the amorphous carbon (denoted as D peak) and graphitic carbon (G peak) [27,35,36]. Typically, the intensity ratio of the D to G peaks is an indicator of the disorder degree [37,38]. The CO-activated catalyst had a lower I_D/I_G than the syngas-activated catalyst, which implies that it produced more graphitized carbon species. More graphitized carbon species would facilitate the carburization of iron species [37], which would improve the generation of FeC_x. The strength of the Fe-O vibration peak diminishes when CO was added to the activated atmosphere and its concentration rises, while the intensity of the D and G peaks increases, which indicates that CO encourages the reduction of FeO_x and the penetration of carbon.

In the Fe 2p spectra (Figure 2a), the activated catalyst both showed the peaks at the binding energies of 711 eV and 725 eV [39], which were attributed to Fe_3O_4. Additionally, the catalysts pretreated with the two CO-bearing gases displayed distinctive peaks ascribed to FeC_x with binding energies of 707 eV and 720 eV [39]. It is worth noting that the peak of metallic iron did not appear in the H_2 pretreated catalyst, which may be due to the oxidation of metallic iron on the surface of the catalyst during the passivation process. In the C 1s spectra (Figure 2b), the Fe–C bond is responsible for the binding energy at 283.58 eV [40]. The carbon content in the Fe–C bond of the CO-activated catalyst was larger

(47%) than that of the syngas-activated catalyst (42.9%), in terms of all carbon species. Graphitic carbon is responsible for the binding energy at 284.58 eV [40], which is somewhat higher in the CO-activated catalyst (30.4%) than in the syngas-activated catalyst (28%). The graphitic carbon peak shifted by 1 eV identified as sp^3-hybridized C [40]. The peak with the highest binding energy (288.6 eV) was associated with carbonates surface species [41].

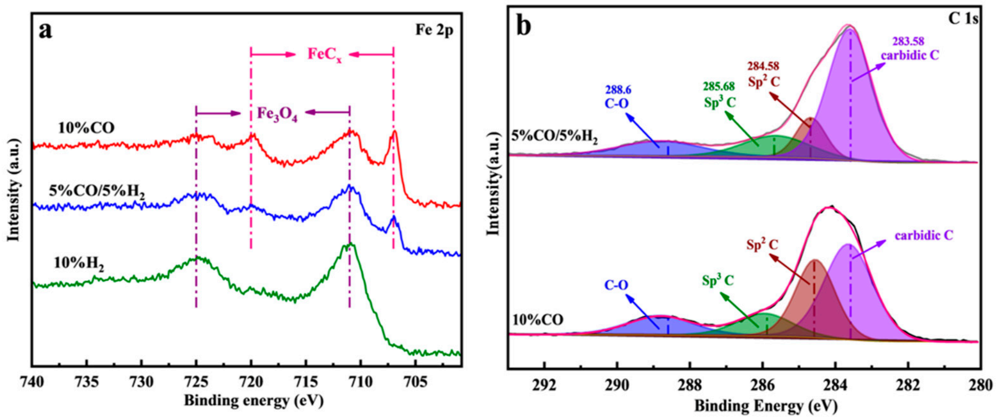

Figure 2. XPS spectra of (**a**) Fe 2p and (**b**) C 1s of the activated catalysts.

The XRD pattern of the activated catalyst is exhibited in Figure 3, and was consistent with the Raman and XPS. All catalysts showed characteristic diffraction peaks of ZnO (JCPDS 79-0207), which originated from the decomposition of $ZnFe_2O_4$. When the activating atmosphere was H_2, the diffraction peaks at 44.7°, 65.1°, and 82.5° were assigned to metallic iron (JCPDS 87-0722), whereas those at 35.4° and 62.5° were attributed to Fe_3O_4 (JCPDS 87-2334). However, for CO and syngas-activated catalysts, in addition to the characteristic peaks of ZnO and Fe_3O_4, the diffraction peaks occurring between 41° and 48° were assigned to iron carbide. However, because of the poor resolution and overlapping patterns of the iron carbide peaks, it was challenging to identify which iron carbide phase was present. Therefore, the specific phase compositions were further determined by MES.

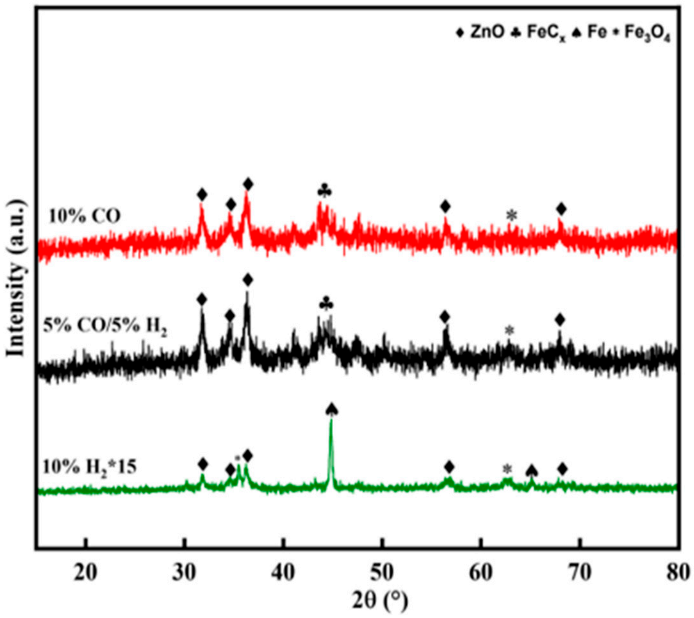

Figure 3. XRD of the activated catalysts.

As shown in Figure S4 and Table 1, according to the MES, the activated catalyst contained several doublets and sextets. The doublets were assigned to the superparamagnetic

Fe^{3+} or Fe^{2+}. The sextets with the Hhf values of 215, 176 and 111 kOe were related to three different sites of stoichiometric χ-Fe_5C_2 [34], and the sextets with the Hhf values of 190 and 329 kOe corresponded to FeC_3 and metallic Fe [15,42]. For the Hhf values of 480 and 447 kOe, which were assigned to the Fe_3O_4 [42], the primary phase in CO and syngas-activated catalysts was FeC_x, which also contains trace amounts of Fe^{2+} or Fe^{3+}. The content of Fe_5C_2 and Fe_3C in CO-activated catalysts were 67.9% and 21%, respectively, while the content of Fe_5C_2 in syngas-activated catalysts and Fe_3C were 77.5% and 9.8%, respectively, which indicates that the iron phase mainly exists in the form of Fe_5C_2. On the contrary, the H_2-activated catalyst had the highest proportion of metallic iron, which is the main form of iron, with a content of 50.2%, followed by Fe_3O_4 with a content of 30.6%.

Table 1. Mössbauer parameters of the activated catalysts.

Catalysts	Phases	MÖSSBAUER Parameters			Area (%)
		IS (mm/s)	QS (mm/s)	Hhf (kOe)	
10% CO	Fe^{3+} (spm)	0.16	0.99		4.3
	Fe^{2+} (spm)	0.87	1.31		6.8
	χ-Fe_5C_2 (I)	0.24	−0.1	214.83	40.1
	χ-Fe_5C_2 (II)	0.16	−0.07	176.92	11.9
	χ-Fe_5C_2 (III)	0.15	0	111.56	15.9
	θ-Fe_3C	0.27	0.13	190.18	21
5% CO/5% H_2	Fe^{2+} (spm)	0.6	1		12.7
	χ-Fe_5C_2 (I)	0.24	−0.1	212.9	34.8
	χ-Fe_5C_2 (II)	0.19	−0.03	179.22	28.5
	χ-Fe_5C_2 (III)	0.24	−0.06	111.66	14.2
	θ-Fe_3C	0.18	−0.06	194.89	9.8
10% H_2	Fe^{3+} (spm)	0.32	0.68		8.8
	Fe^{2+} (spm)	0.89	0.95		10.2
	Fe_3O_4 (A)	0.29	−0.05	480.18	6.7
	Fe_3O_4 (B)	0.62	0	447.09	23.9
	Fe	0	0	329.11	50.3

The surface carbon deposits of the pretreated catalysts were analyzed using a thermogravimetric analyzer (TGA). The TGA curve can be divided into three stages. As shown in Figure 4a,b, the weight loss in the first stage was the removal of bound water, FeC_x oxidation causes the weight growth in the second stage, and the oxidation of carbon deposits causes the final weight loss. The weight gain ratio of the catalyst after CO activation in the second stage (12.9%) was significantly higher than that of the catalyst after syngas activation (10.2%), which indicates that the content of FeC_x species in the catalyst after CO activation was more than that of the catalyst after syngas activation. It is worth noting that the CO-activated catalyst had less weight loss (6.4%) at lower combustion temperature (354.7 °C) (Figure S5a), while the syngas-activated catalyst had more severe carbon deposition (7.1%) and correspondingly higher combustion temperature (358.5 °C) (Figure S5b). This indicates that the CO-activated catalyst better maintains the CO dissociation and carburization process.

The average particle size and morphology of the activated catalyst were observed by TEM. As depicted in Figure 5a–c, compared with the fresh catalyst, the average particle size of the activated catalyst was significantly larger, among which, the average particle size of the H_2-activated catalyst was the largest, while the average particle size of the CO and syngas-activated catalysts was relatively high. This may be due to the fact that H_2 promotes particle agglomeration and sintering. Additionally, because Fe_3O_4 has a lower density than FeC_x, which allows carbides from the splitting of Fe_3O_4, it is also likely that the particle size of FeC_x was less than that of Fe_3O_4 [43,44]. As shown in Figure S6 of the Supplementary Materials, for the CO-activated particle, the lattice spacing is 0.192 nm, consistent with the (221) facet of Fe_5C_2. For the syngas-activated particle, the lattice spacing is 0.214 nm, consistent with the (202) facet of Fe_5C_2. The CO-activated and syngas-activated catalysts display the lattice fringe of 0.246 nm, corresponding to the (121) plane of Fe_3C. For the H_2-activated particle, the lattice spacing is 0.248 nm and 0.21 nm, consistent with the (311) facet of Fe_3O_4 and the (100) plane of Fe. The results from XRD and MES are in accordance with the observations.

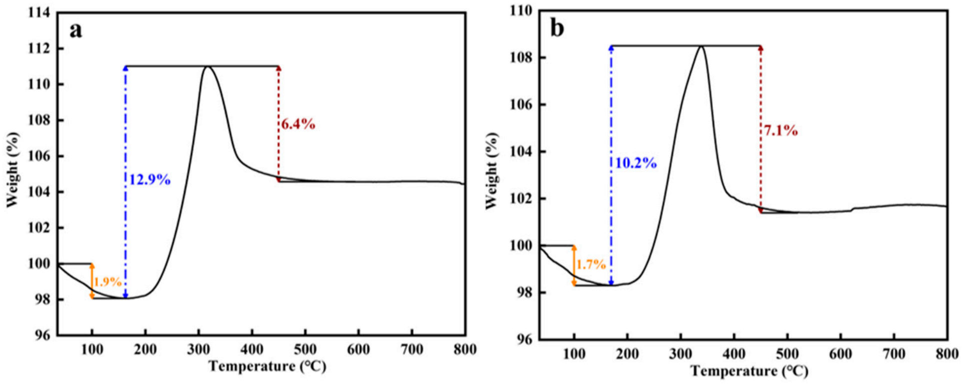

Figure 4. TG curves of the (**a**) 10% CO and (**b**) 5% CO/5% H_2-activated catalysts.

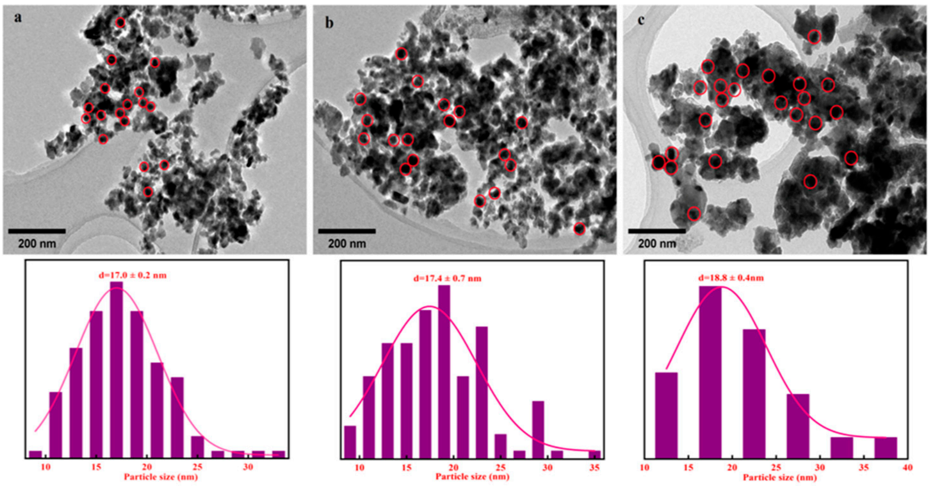

Figure 5. TEM images and particle size distribution of the (**a**) 10% CO-, (**b**) 5%CO/5%H_2-, and (**c**) 10%H_2-activated catalysts.

2.4. Structure and Properties of Spent Catalysts

Taking into account the differences between catalysts pretreated with different atmospheres, the structure and phase compositions of the spent catalysts were further examined by Raman, XPS, XRD, and MES. As illustrated in Figure 6a, the spent catalysts pretreated with H_2 also have vibrational peaks at 1350 cm^{-1} and 1590 cm^{-1} ascribed to carbon deposition, which indicates that carburization occurred during the reaction and FeC_x was generated.

The XPS results are displayed in Figure 6b. The Fe $2p_{3/2}$ peak at the binding energy of 707.3 eV refers to FeC_x, and the locations at 710.1 eV and 712.1 eV correspond to Fe^{2+} and Fe^{3+} in iron oxides, respectively [45,46]. A_{FeCx}/A_{total} represents the proportion of FeC_x to total iron species on the catalyst surface. The A_{FeCx}/A_{total} of the catalyst for the syngas pretreatment was the lowest (0.03), and the A_{FeCx}/A_{total} of the catalyst for the H_2 pretreatment was the highest (0.15). It is possible that the syngas pretreatment catalyst's surface carbon was relatively severe after the reaction, which interferes with the ability to identify FeC_x species. Furthermore, metallic iron might be more conducive to the dissociation of CO_2 and the penetration of carbon than FeO_X, thereby increasing the content of FeC_X. The A_{FeCx}/A_{total} of the catalyst for the syngas pretreatment and the CO pretreatment catalyst (0.11) were essentially equivalent.

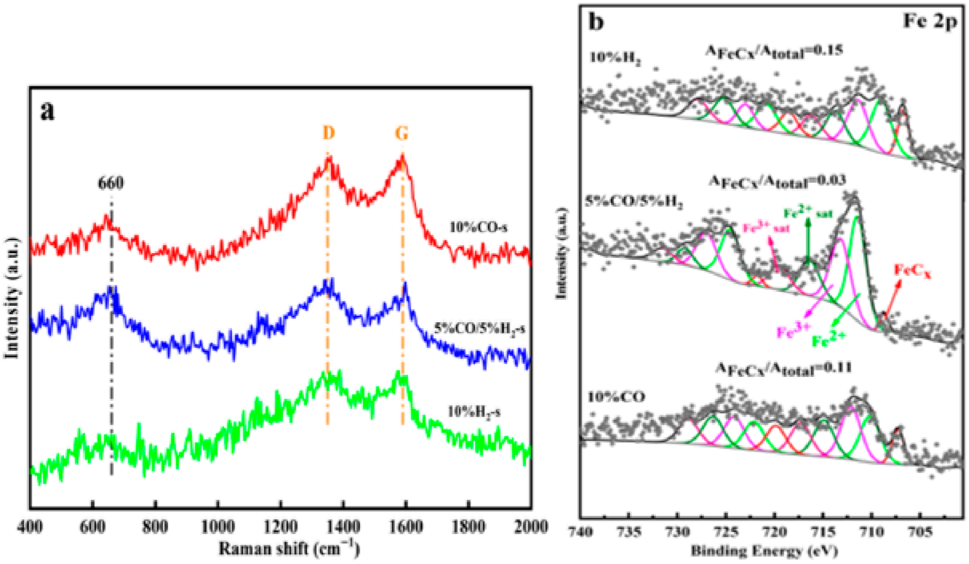

Figure 6. (**a**) Raman and (**b**) XPS spectra of Fe 2p of the spent catalysts.

As depicted in Figure 7, for the spent catalyst of H_2 pretreatment, the diffraction peaks appeared between 41° and 48°, which were assigned to FeC_x, while metallic iron diffraction peaks vanished, indicating that metallic iron was transformed into FeC_x during the reaction. In contrast to the following activation, the catalyst phase for CO and syngas pretreatment catalysts remained mostly unchanged after the reaction. The composition of the particular phase should be further determined by MES.

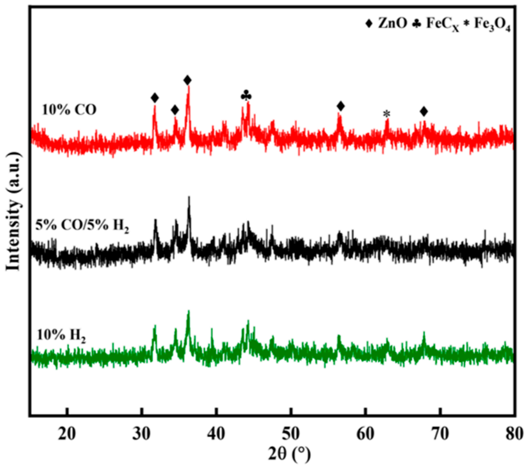

Figure 7. XRD of the spent catalysts.

As illustrated in Figure S7 and Table 2, the spent catalysts with varied pretreatment atmospheres contained one doublet and four sextets. The superparamagnetic (spm) Fe^{2+} was responsible for the doublet with IS values of 0.4, 0.52, and 0.64 $mm{\cdot}s^{-1}$, which was increased in comparison to the activated catalyst of CO and syngas pretreatment catalysts. The proportion of FeC_x dropped, indicating that the reaction caused FeC_x to be oxidized. The contents of Fe_5C_2 and FeC_3 for the spent catalyst of CO pretreated were 64.6% and 19%, 76.3% and 8.2% for the syngas pretreated, and 78.9% and 12.2% for the H_2 pretreated, respectively.

Table 2. Mössbauer parameters of the spent catalysts.

Catalysts	Phases	MÖSSBAUER Parameters			Area (%)
		IS (mm/s)	QS (mm/s)	Hhf (kOe)	
10% CO	Fe^{2+} (spm)	0.52	1.02		16.4
	χ-Fe_5C_2 (I)	0.24	−0.13	217.12	30.6
	χ-Fe_5C_2 (II)	0.19	−0.01	179.72	18.5
	χ-Fe_5C_2 (III)	0.2	0	113.89	15.5
	θ-Fe_3C	0.22	0.03	194.35	19
5% CO/5% H_2	Fe^{2+} (spm)	0.4	0.79		15.5
	χ-Fe_5C_2 (I)	0.24	−0.12	216.03	33.5
	χ-Fe_5C_2 (II)	0.18	−0.01	180.95	26.8
	χ-Fe_5C_2 (III)	0.22	−0.06	113.16	16
	θ-Fe_3C	0.19	−0.07	195.71	8.2
10% H_2	Fe^{2+} (spm)	0.64	0.9		8.8
	χ-Fe_5C_2 (I)	0.24	−0.1	216.73	37
	χ-Fe_5C_2 (II)	0.19	−0.02	181.77	27.6
	χ-Fe_5C_2 (III)	0.23	−0.05	113.41	14.3
	θ-Fe_3C	0.17	−0.07	197.69	12.2

The thermogravimetric results of the spent catalysts are depicted in Figures 8a–c and S8a–c. Carbon deposition was the most severe for syngas pretreatment catalysts (9.7%) and mildest for hydrogen pretreatment catalysts (1.5%), possibly due to the faster carburization rate of metallic iron compared to iron oxides [47], accelerating the consumption of carbon species. The oxidation of FeC_X was responsible for the weight gain at the second stage of the curve, and the order was H_2-pretreated > CO-pretreated > syngas-pretreated, proving that metallic iron has a greater carburizing ability. This may be because the removal of O during the carburization of FeO_X slowed the rate of carbonization, whereas the carburization of metallic iron was a comparatively simple process.

In situ DRIFTS was employed to investigate the adsorbed species and reaction intermediates on the catalyst surface in reaction conditions after different atmospheres' pretreatments (Figure 9a–c). After reaching the reaction temperature, the bands attributed to bicarbonate species (HCO_3*, ca. 1395 and 1611 cm^{-1}), gaseous CO (ca. 2100 and 2170 cm^{-1}) and the vibration of C-H in CH_4 (ca. 3009 cm^{-1}) were detected in all catalysts [15,34]. Only the CO pretreated and syngas pretreated catalysts showed the peaks at 2861 cm^{-1} and 2927 cm^{-1}, which were attributed to -CH_2 group, and the band at 2958 cm^{-1}, that was ascribed to C-H in -CH_3 group [48–50]. Compared to syngas pretreatment catalysts, the peak intensity at these positions was noticeably stronger for CO pretreatment catalysts due to the fact that -CH_2 and -CH_3 groups were important species for C–C coupling to generate C_{2+} hydrocarbons. This was in accordance with the catalyst for CO pretreatment having the greatest selectivity towards C_{5+} hydrocarbons. In addition, only the CO-pretreated and syngas-pretreated catalysts showed the C=C band of π-bonded CH_2=CH_2 at 1710 cm^{-1} and the C-H stretching of alkenes [51–53], and these bands in the CO pretreated catalysts were stronger. This may account for the highest C_2–C_4 olefin selectivity and O/P of the CO pretreatment catalyst.

It is worth noting that the initial O/P of the H_2 pretreated catalyst was high and then gradually decreased, while the trend of CO and syngas pretreated catalyst was the opposite. This may be due to the fact that the initial phases of the H_2 pretreated catalyst were mainly Fe and Fe_3O_4, which have a relatively strong dissociation ability for CO_2, but a weak dissociation ability for H_2, consistent with the absence of C-H peaks in the in situ DRIFTS. At the same time, the low H concentration on the surface was not conducive to the secondary hydrogenation, so the initial O/P was high. With the formation of FeC_X, the dissociation of H_2 gradually increased, so the O/P gradually decreased. On the contrary, the initial phases of the catalyst for CO and syngas pretreated contained a large amount of FeC_X, which has a strong dissociation ability for CO_2 and H_2, and the H concentration on the surface was higher, so the initial O/P was lower. As the reaction proceeded, FeC_X was oxidized to Fe_3O_4, which weakened the dissociation of H_2, and O/P gradually increased.

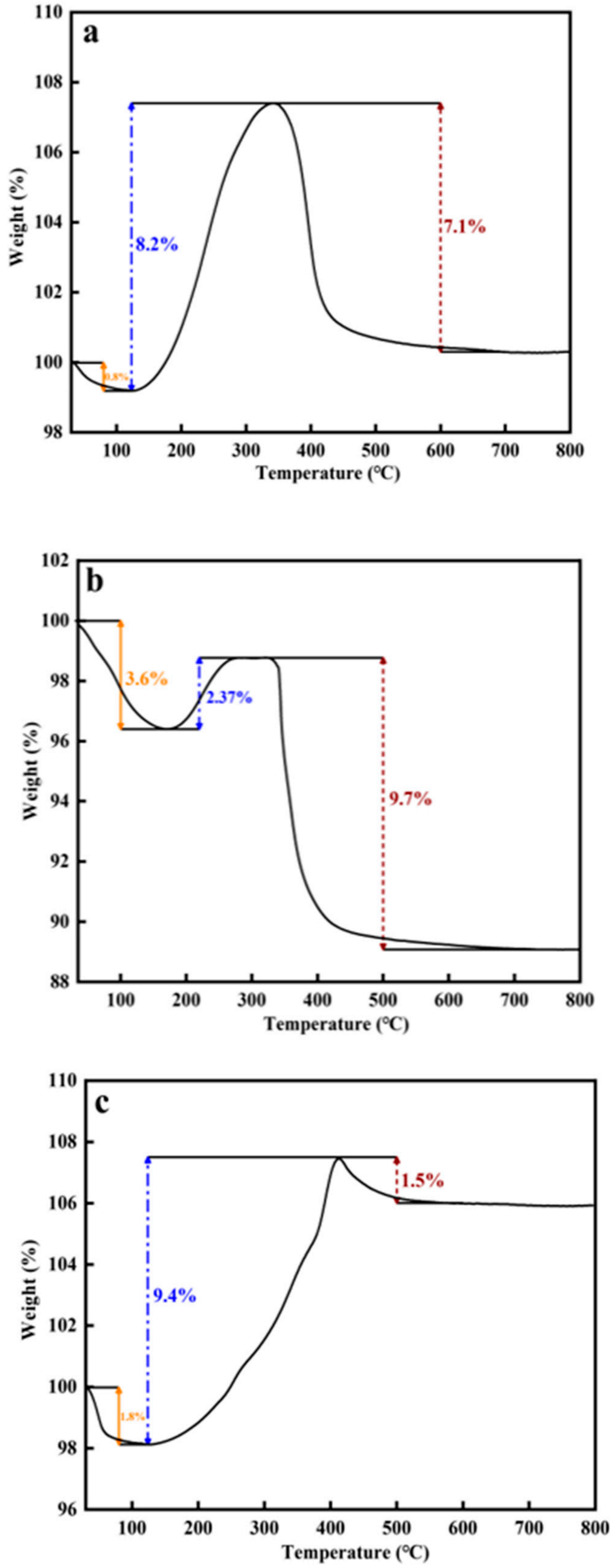

Figure 8. TG curves of the spent catalysts of (**a**) 10%CO-, (**b**) 5%CO/5%H_2- and (**c**) 10%H_2-pretreated.

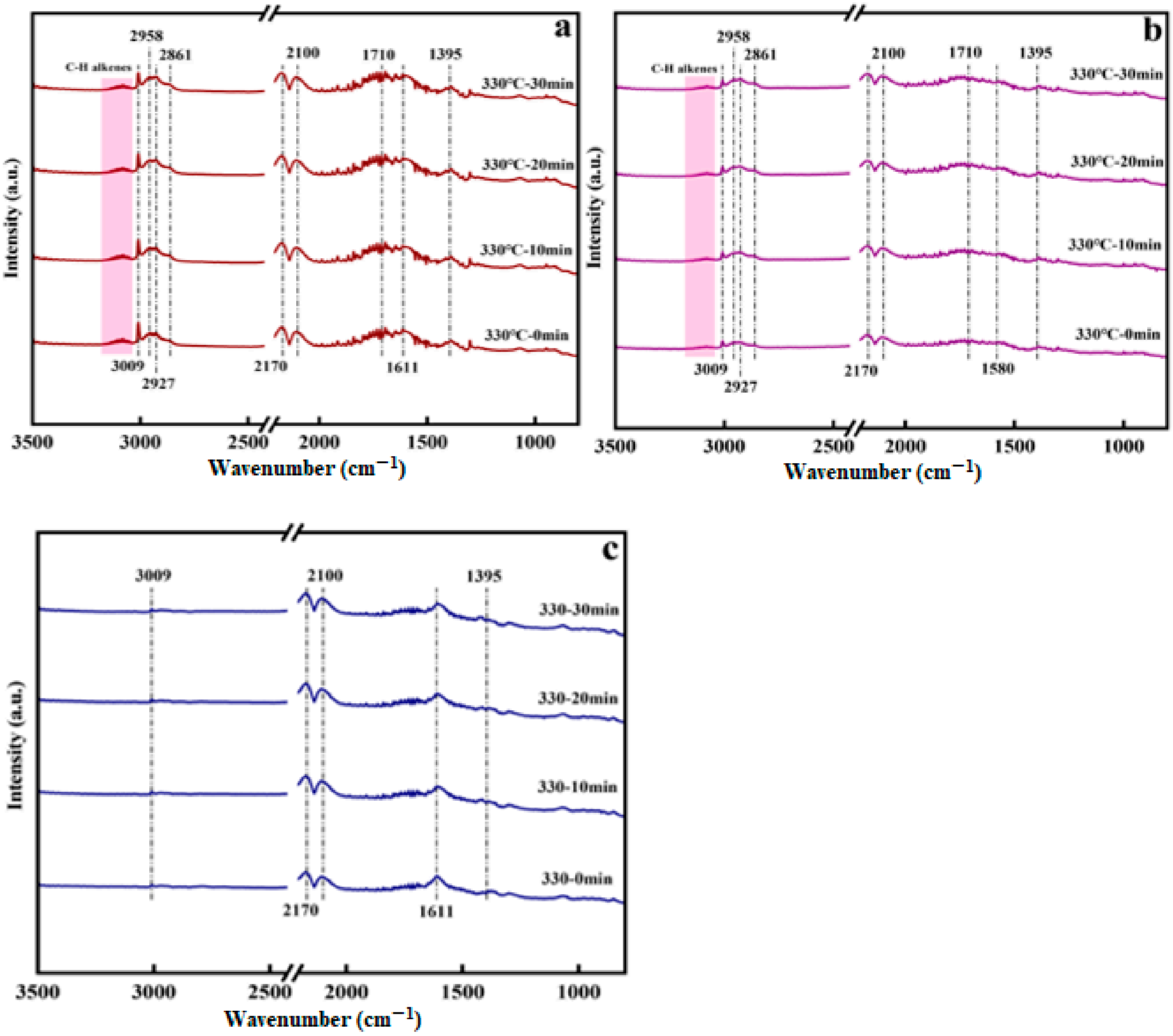

Figure 9. In situ DRIFTS spectra of CO_2 hydrogenation over the catalysts activated by (**a**) 10% CO, (**b**) 5% CO/5% H_2 and (**c**) 10% H_2.

The absence of an olefin signal in the DRIFTS analysis of the H_2-pretreated catalyst can be ascribed to the lack of FeCx phases during the initial stage of the reaction. Furthermore, the greater particle size of the H_2-pretreated catalyst (as seen in Figure 5) compared to CO- or syngas-pretreated catalysts is another reason for its low initial activity.

As illustrated in Figure S9a,b, C_2H_4 and C_3H_6 were employed as model olefins to investigate olefin desorption on the spent catalyst. There are two desorption peaks for C_3H_6-TPD, the peak centers at 90, 100, and 148 °C were physical adsorption [31]. The peaks above 460 °C were chemisorption [31], which dropped from 479 °C to 466 °C, indicating that the CO pretreatment catalyst was more conducive to C_3H_6 desorption. Only chemisorption with a desorption temperature above 480 °C arose in C_2H_4-TPD, and the peak centers were located at 482, 484, and 489 °C [54], with a trend of change consistent with that of C_3H_6-TPD. This indicates that the CO pretreatment catalyst was more beneficial to olefin desorption, thereby enhancing olefin selectivity.

2.5. Structure-Performance Relationship

A series of characterization and performance tests on activated and spent catalysts demonstrated that pretreatment atmospheres have a significant impact on catalyst performance in CO_2 hydrogenation, which can be briefly summarized as follows (Figure S10). In the H_2-pretreated catalyst, the iron phase was mostly reduced to metallic iron, while particle aggregation and sintering occurred. The fresh catalyst was pretreated with CO and syngas, iron carbides appeared, mainly Fe_5C_2 and Fe_3C, and the content of Fe_5C_2 was higher than that of Fe_3C. The content of Fe_5C_2 in the syngas-pretreated catalyst was higher than the CO-pretreated catalyst, which could be due to the addition of H_2 to promote CO dissociation and increase the carbonization rate, which in turn promoted the formation of carbon-rich Fe_5C_2 [55], but the content of Fe_3C in the CO-pretreated catalyst was higher. Fe_3C as the active phase was beneficial to the formation of C_2–$C_4^=$ and C_{5+} hydrocarbons [56–58], which was also proved by the in situ DRIFTS.

According to the Raman analysis, the surface of the H_2 pretreatment catalyst primarily consisted of FeO_X, whereas that of the CO and syngas pretreatment catalyst typically consisted of FeO_X and carbon deposition. The results of the XPS confirmed the existence of FeO_X on the surface of three different atmosphere pretreatment catalysts, and Fe_3O_4 was the main form. At the same time, FeC_x also appeared on the CO and syngas pretreatment catalysts, which corresponded to the carbon deposition in the Raman results, indicating that the catalysts had experienced carburization. The MES results further confirmed the existence of the iron phase form, and clarified that the FeC_x in CO and syngas pretreatment catalysts were mainly Fe_3C and Fe_5C_2, between which Fe_3C was conducive to the formation of C_2–$C_4^=$ and C_{5+} hydrocarbons, also consistent with the optimal performance of the CO-pretreated spent catalyst with the highest Fe_3C content.

The H_2-pretreated catalyst demonstrated a high O/P ratio at the beginning of the reaction and then flattened out with time-on-stream, manifesting a significant phase transition in the initial stage of the reaction. The phase transition can be explained as the variation in surface hydrogen/carbon balance. The H_2 pretreated catalyst had a high hydrogen coverage and a low carbon coverage at the initial stage, which favored the hydrogen-assisted CO_2 adsorption to generate bicarbonate species as evidenced in the in situ DRIFTS study (Figure 9). These bicarbonate species can further undergo step hydrogenation to form CO*, which can be dissociated on the catalyst surface to generate free carbons to drive carburization and CH_x species to initiate C–C coupling reaction. As the reaction proceeds, the hydrogen coverage decreases rapidly, which may retard hydrogenation reaction since the adsorption of gaseous hydrogen is required. On the other hand, the sluggish hydrogenation rate may shift the surface H/C balance towards a carbon-rich surface, thus enhancing the carburization process. The carburization reaction involves the permeation of free carbons into the bulk iron, which is expected to occur at a much slower rate than the surface C–C coupling reactions. As the reaction continues, the formation of free CH_x species is slowed due to rapid consumption of adsorbed hydrogen, while the carbon accumulation varies in the opposite way. The observed trend for O/P ratio suggests a dynamic balance of carburization and hydrogenation.

In contrast to the H_2-pretreated catalyst, the surface free carbon concentration of CO and syngas-pretreated catalysts was higher, resulting in a faster dissociation rate of H_2 in reaction gas than CO_2 dissociation rate at the initial reaction stage. The relatively high hydrogen coverage on the surface of the catalyst was conducive to the formation of $-CH_2$ and $-CH_3$ intermediates, which further undergo C–C coupling to generate long-chain hydrocarbons. The bulk phase of CO and syngas-pretreated catalysts consisted mostly of iron carbide, and the content of Fe_3O_4 was very low, which was not conducive to the RWGS reaction. As the reaction continued, the free carbon on the surface either combined with hydrogen or penetrated into the bulk phase and combined with iron, and was gradually consumed. At the same time, the oxidation of FeC_x by the water and CO_2 increased the iron oxide content, which further accelerated the RWGS reaction.

When compared to the activated catalyst, the FeC_X content of the CO-pretreated and syngas-pretreated spent catalysts decreased while the FeO_X content increased, and carbon deposition was exacerbated, indicating that carbonization and oxidation happened parallelly during CO_2 hydrogenation. The lowest activity of the H_2-pretreated spent catalyst may be due to the relatively small FeO_X content, which was not conducive to the occurrence of the RWGS. The CO-pretreated spent catalyst had the highest FeO_X and Fe_3C contents, and the carbon deposition was relatively mild, which was conducive to maintaining the oxidation and carbonization balance. The high FeO_X content was beneficial to the occurrence of RWGS. FeC_3 promotes Fischer–Tropsch synthesis (FTS) and also drives the progression of RWGS. Thus, the CO-pretreated spent catalyst had the highest activity, which favors the formation of olefins and C_{5+} hydrocarbons.

3. Materials and Methods

3.1. Catalyst Preparation

Bulk Fe-Zn-Na (molar ratio of Fe:Zn = 2:1) catalyst was prepared via a co-precipitation at room temperature, as described in our previous work [34]. Briefly, a certain amount of $FeCl_3 \bullet 6H_2O$ (Analytical Reagent) and $ZnCl_2$ (Analytical Reagent), which obtained from Sinopharm Chemical Reagent (Shanghai, China), was weighed and dissolved in ethylene glycol to create a mixed solution. The solution was then transferred to a beaker and agitated for 30 min at room temperature. A sodium carbonate solution was slowly added dropwise to the Fe-Zn precursor solution while stirring. The resultant precipitate was recovered by centrifugation and washed with deionized water multiple times. The resultant slurry was dried at 60 °C overnight, and calcined at 450 °C (heating rate 2 °C/min) for 4 h in a muffle furnace (Figure S11).

3.2. Pretreatment and Evaluation of Catalyst

The CO_2 hydrogenation was carried out in a stainless-steel fixed bed reactor with an internal diameter of 6 mm and a length of 400 mm. A 25 mg sample diluted with 75 mg of silicon carbide was then placed in the isothermal zone of the tubular reactor. The catalyst was temperature-programed heated under three different reductive gases (10% CO/90% Ar, 5% CO/5% H_2/90% Ar or 10% H_2/90% Ar) at 350 °C (heating rate 2 °C/min) with a gas flow rate of 25 mL/min under atmospheric pressure for 5 h. Then, the reactor was cooled down to 330 °C and pressurized to 1.5 MPa with the reactant gas (20% CO_2/60% H_2/20% N_2, GHSV = 60,000 $mL \cdot g_{cat}{}^{-1} \cdot h^{-1}$) The gaseous products were analyzed by an online gas chromatograph (GC, Clarus 580, PerkinElmer, Waltham, MA, USA) equipped with a thermal conductivity detector (TCD) and a flame ionization detector (FID). H_2, N_2, CO, and CO_2 were analyzed by a TDX-01 column connected to TCD and the hydrocarbons were analyzed by a capillary column (Agilent HP-Plot Q) connected to FID. The liquid products were collected in a cold trap and analyzed offline using an GC-MS (GC(7890A)-MS(5975C), Agilent Technologies Inc., Santa Clara, CA, USA) equipped with a PONA column. A carbon balance of over 92% was established for all catalytic performance tests. The catalyst samples after reductive pretreatment and reaction were carefully collected without air exposure and then passivated with 1%O_2/99%Ar at room temperature for 15 min [59].

CO_2 conversion (X_{CO_2}) was calculated by Equation (1):

$$X_{CO_2} = \frac{CO_{2,in} - CO_{2,out}}{CO_{2,in}} \times 100\% \quad (1)$$

where $CO_{2,in}$ and $CO_{2,out}$ represent the moles of CO_2 inlet and outlet, respectively.

The selectivity of hydrocarbon (S_{C_i}) in gaseous products was calculated by Equation (2):

$$S_{C_i} = \frac{\text{Mole of } C_i \times i}{\text{Mole of CO} + \sum_{i=1}^{7} i \times \text{Mole of } C_i} \times 100\% \quad (2)$$

CO selectivity (S_{CO}) was calculated according to Equation (3):

$$S_{CO} = \frac{\text{Mole of CO}}{\text{Mole of CO} + \sum_{i=1}^{7} i \times \text{Mole of } C_i} \times 100\% \quad (3)$$

The selectivity of hydrocarbon (L_{C_i}) in liquid products was calculated by Equation (4):

$$L_{C_i} = \frac{L_{C_i} \text{ area percentage by MS} \times i}{\sum L_{C_i} \text{area percentage by MS} \times i} \tag{4}$$

The space time yield (STY) was calculated by Equation (5):

$$\text{STY}\left(\text{mmol}_C \cdot g_{Fe}{}^{-1} \cdot h^{-1}\right) = \frac{Q_{in} \times V_{CO_2} \times X_{CO_2}}{V_m \times m_{Fe}} \times S_{C_{2-7\ \alpha-\text{olefins}}} \tag{5}$$

where Q_{in} is the total volume flow rate of the inlet reactant gas, mL/h. V_{CO_2} is the proportion of CO_2 in the inlet reactant gas, and V_m represents the molar volume of an ideal gas at standard temperature and pressure, V_m = 22.4 mL/mmol.

3.3. Characterization Methods

The elemental composition of the catalyst was analyzed by inductively coupled plasma optical emission spectrometer (ICP-OES, 725, Agilent Technologies Inc., Santa Clara, CA, USA).

The Raman spectra were recorded on a confocal Raman spectrometer (LabRAM HR, Horiba J.Y., Paris, France) equipped with a visible 633 nm Ar^+ laser and 325 nm Ar^+ laser and high-grade Leica microscopes (long working distance objective 50× and 20×, respectively). The Raman peak of single-crystal silicon at 520.7 cm^{-1} was used for calibration. For all samples, the test conditions were set to 200 μm confocal pore size, 20 s exposure time, 1 mW irradiation intensity, and attenuated by a factor of 10 to avoid damaging samples. The signal was collected at 180° (back scattering plane) by a CCD array detector (1024 × 256 pixels, 26 mm in size).

The bulk crystalline structures of all samples were determined by XRD (D8 Advance, Bruker, Karlsruhe, Germany) using a Cu Kα monochromatized radiation source (k = 1.5418 Å) at 40 kV and 40 mA. The scanning speed was 5° min^{-1} in a 2θ angle range of 5–90°.

The ^{57}Fe Mössbauer spectroscopy (MES) was performed on an electromechanical spectrometer (Wissel 1550, Wissenschaftliche Elektronik GmbH, Starnberg, Germany) equipped with a ^{57}Co/Pd irradiation source at room temperature. The velocity was calibrated by a 25 μm-thick α-Fe foil, and the isomer shift (IS) was referenced to α-Fe at room temperature.

The particle size and morphology were determined by a transmission electron microscope (JEOL JEM 2100F, JEOL, Akishima, Japan) (accelerating voltage = 200 kV). The average particle size was determined by measuring more than 200 nanoparticles.

Temperature-programmed desorption of C_2H_4, C_3H_6 (C_2H_4, C_3H_6-TPD) was conducted in a micro fixed-bed reactor connected to a mass spectrometer (HPR-20, Hiden Analytical, Britain). The catalyst was first treated at 250 °C for 2 h to remove the bound water from the sample under pure Ar. After lowering to room temperature, the surface oxide layer was removed by treatment with 10% CO at 350 °C for 2 h. Subsequently, the temperature was reduced to room temperature while the residual CO was purged by pure Ar, and then the adsorption species were switched in the reactor for 2 h. After that, a stable baseline was obtained on the MS by pure Ar purging. The catalysts were heated from room temperature to 800 °C at 10 °C/min. Mass of m/z = 26 (C_2H_4), 41 (C_3H_6) was monitored.

Thermogravimetric (TG) analysis was performed on a TG analyzer (Rigaku DTA8122, Rigaku, Tokyo, Japan) with a heating rate of 10 °C/min from room temperature to 800 °C in air condition.

In situ DRIFT spectra were recorded on a Frontier spectrometer (Spectrum 100, PerkinElmer, Waltham, MA, USA) equipped with a Harrick Praying Mantis diffuse reflection cell and a mercury cadmium telluride (MCT) detector cooled by liquid nitrogen. The catalyst sample was pretreated using different reductive gases at 350 °C and 1 bar for 5 h. Then, the temperature was lowered to 330 °C and the pressure was set to 1.5 MPa under Ar flow and a background spectrum was recorded. The pretreated sample was next exposed to a reactant gas mixture containing 20 vol. % CO_2, 60 vol. % H_2, and 20 vol. % Ar with a total gas flow of 25 mL/min for 30 min. The DRIFT spectra were collected at 4 cm^{-1} resolution and 64 scans.

4. Conclusions

In conclusion, we investigated the impact of different pretreatment atmospheres on the performance of iron-based catalysts in CO_2 hydrogenation, using various characterizations such as Raman, XPS, MES, TG and in situ DRIFTS, on the activated and spent catalysts. Our results indicated that the differences in the performance of the spent catalysts were primarily due to differences in iron phase composition and carbon deposition. Specifically, based on the analysis of the results from MES and Raman, we found that the H_2-pretreated catalyst had low activity due to the lack of FeO_X, while the CO-pretreated catalyst had the highest content of Fe_3C and FeO_X, resulting in the highest activity and selectivity to olefins and C_{5+} hydrocarbons. Additionally, the TG findings demonstrated that the catalyst's performance was somewhat impacted by the degree of carbon deposition. For instance, the mild degree of carbon deposition in the CO-pretreated catalyst contributed to maintaining the balance of FeC_X and FeO_X, resulting in continuous optimal performance. At the same time, it can be seen from the TEM results that the sintering and agglomeration of the catalyst were not conducive to the exposure of the active sites and inhibited the reactivity of the catalyst. The results of in situ DRIFTS showed that the CO pretreatment catalyst was more conducive to the formation of olefins and -CH_2, -CH_3 groups in the early stage of the reaction, which together with the composition results of the bulk and surface phase of MES, XRD, Raman and XPS, explain the CO pretreatment catalyst for optimum performance. Finally, the results of TPD also showed that the CO pretreatment catalyst was more conducive to the desorption of light olefins and improved the selectivity of olefins. These findings suggest a novel strategy for in the future selecting and optimizing the pretreatment atmosphere in the CO_2 hydrogenation process.

Supplementary Materials: The following supporting information can be downloaded at: https://www.mdpi.com/article/10.3390/catal13030594/s1, Figure S1: 100 h time on stream of the Fe_2Zn_1 activated by (**a**) 5% CO/5% H_2/Ar and (**b**) 10% H_2/Ar and 100 h liquid product analysis of the Fe_2Zn_1 activated by (**c**) 5% CO/5% H_2/Ar and (**d**) 10% H_2/Ar under reaction conditions (330 °C, 1.5 MPa, 60,000 $mL \cdot g^{-1} \cdot h^{-1}$); Figure S2: (**a**) XRD, (**b**) Raman, and (**c**) TEM of the fresh catalyst; Figure S3: Raman of the activated catalysts; Figure S4: Mössbauer spectra of the activated catalysts; Figure S5: DTG curves of the (**a**) 10% CO- and (**b**) 5% CO/5% H_2-activated catalysts; Figure S6: HRTEM images of the (**a**,**d**) 10% CO-, (**b**,**e**) 5% CO/5% H_2-, (**c**,**f**) 10% H_2-activated catalysts; Figure S7: Mössbauer spectra of the spent catalysts; Figure S8: DTG curves of the spent catalysts of (**a**) 10%CO-, (**b**) 5% CO/5% H_2- and (**c**) 10% H_2-pretreated; Figure S9: (**a**) C_2H_4-TPD and (**b**) C_3H_6-TPD of the spent catalysts; Figure S10: Structural and phase composition of the catalyst after pretreatment and reaction; Figure S11: Schematic representation of the catalysts preparation.

Author Contributions: Data curation, formal analysis, conceptualization, investigation and writing original draft, Y.P.; formal analysis, X.D.; conceptualization, C.Z.; supervision, M.Z.; funding acquisition, project administration, supervision and writing—review and editing, Z.Y. and Y.-F.H. All authors have read and agreed to the published version of the manuscript.

Funding: The National Science Foundation of China (22278405, 22238003).

Data Availability Statement: Data will be made available upon request.

Acknowledgments: We gratefully thank the funding support from the National Science Foundation of China (22278405, 22238003) for this work.

Conflicts of Interest: The authors declare no conflict of interest.

References

1. Jiang, B.; Xia, D.; Yu, B.; Xiong, R.; Ao, W.; Zhang, P.; Cong, L. An environment-friendly process for limestone calcination with CO_2 looping and recovery. *J. Clean. Prod.* **2019**, *240*, 118147. [CrossRef]
2. Porosoff, M.D.; Yan, B.; Chen, J.G. Catalytic reduction of CO_2 by H_2 for synthesis of CO, methanol and hydrocarbons: Challenges and opportunities. *Energy Environ. Sci.* **2016**, *9*, 62–73. [CrossRef]
3. Ma, Z.; Porosoff, M.D. Development of Tandem Catalysts for CO_2 Hydrogenation to Olefins. *ACS Catal.* **2019**, *9*, 2639–2656. [CrossRef]
4. Gao, X.; Atchimarungsri, T.; Ma, Q.; Zhao, T.-S.; Tsubaki, N. Realizing efficient carbon dioxide hydrogenation to liquid hydrocarbons by tandem catalysis design. *EnergyChem* **2020**, *2*, 100038. [CrossRef]
5. Wei, J.; Yao, R.; Han, Y.; Ge, Q.; Sun, J. Towards the development of the emerging process of CO_2 heterogenous hydrogenation into high-value unsaturated heavy hydrocarbons. *Chem. Soc. Rev.* **2021**, *50*, 10764–10805. [CrossRef] [PubMed]
6. Yan, C.; Wang, C.-H.; Lin, M.; Bhalothia, D.; Yang, S.-S.; Fan, G.-J.; Wang, J.-L.; Chan, T.-S.; Wang, Y.-l.; Tu, X.; et al. Local synergetic collaboration between Pd and local tetrahedral symmetric Ni oxide enables ultra-high-performance CO_2 thermal methanation. *J. Mater. Chem. A* **2020**, *8*, 12744–12756. [CrossRef]
7. Bhalothia, D.; Hsiung, W.-H.; Yang, S.-S.; Yan, C.; Chen, P.-C.; Lin, T.-H.; Wu, S.-C.; Chen, P.-C.; Wang, K.-W.; Lin, M.-W.; et al. Submillisecond Laser Annealing Induced Surface and Subsurface Restructuring of Cu–Ni–Pd Trimetallic Nanocatalyst Promotes Thermal CO_2 Reduction. *ACS Appl. Energy Mater.* **2021**, *4*, 14043–14058. [CrossRef]
8. Wei, J.; Ge, Q.; Yao, R.; Wen, Z.; Fang, C.; Guo, L.; Xu, H.; Sun, J. Directly converting CO_2 into a gasoline fuel. *Nat. Commun.* **2017**, *8*, 15174. [CrossRef]
9. Dorner, R.W.; Hardy, D.R.; Williams, F.W.; Willauer, H.D. Heterogeneous catalytic CO_2 conversion to value-added hydrocarbons. *Energy Environ. Sci.* **2010**, *3*, 884–890. [CrossRef]
10. Zhuang, Y.; Currie, R.; McAuley, K.B.; Simakov, D.S.A. Highly-selective CO2 conversion via reverse water gas shift reaction over the 0.5 wt% Ru-promoted $Cu/ZnO/Al_2O_3$ catalyst. *Appl. Catal. A Gen.* **2019**, *575*, 74–86. [CrossRef]
11. Gu, M.; Dai, S.; Qiu, R.; Ford, M.E.; Cao, C.; Wachs, I.E.; Zhu, M. Structure–Activity Relationships of Copper- and Potassium-Modified Iron Oxide Catalysts during Reverse Water–Gas Shift Reaction. *ACS Catal.* **2021**, *11*, 12609–12619. [CrossRef]
12. Widmann, D.; Behm, R.J. Active oxygen on a Au/TiO_2 catalyst: Formation, stability, and CO oxidation activity. *Angew. Chem. Int. Ed. Engl.* **2011**, *50*, 10241–10245. [CrossRef]
13. Goguet, A.; Meunier, F.C.; Tibiletti, D.; Breen, J.P.; Burch, R. Spectrokinetic Investigation of Reverse Water-Gas-Shift Reaction Intermediates over a Pt/CeO_2 Catalyst. *J. Phys. Chem. B* **2004**, *108*, 20240–20246. [CrossRef]
14. Bhalothia, D.; Yang, S.-S.; Yan, C.; Beniwal, A.; Chang, Y.-X.; Wu, S.-C.; Chen, P.-C.; Wang, K.-W.; Chen, T.-Y. Surface anchored atomic cobalt-oxide species coupled with oxygen vacancies boost the CO-production yield of Pd nanoparticles. *Sustain. Energy Fuels* **2023**, *7*, 526–536. [CrossRef]
15. Xu, M.; Liu, X.; Cao, C.; Sun, Y.; Zhang, C.; Yang, Z.; Zhu, M.; Ding, X.; Liu, Y.; Tong, Z.; et al. Ternary Fe–Zn–Al Spinel Catalyst for CO_2 Hydrogenation to Linear α-Olefins: Synergy Effects between Al and Zn. *ACS Sustain. Chem. Eng.* **2021**, *9*, 13818–13830. [CrossRef]
16. Li, S.; Yang, J.; Song, C.; Zhu, Q.; Xiao, D.; Ma, D. Iron Carbides: Control Synthesis and Catalytic Applications in CO_x Hydrogenation and Electrochemical HER. *Adv. Mater.* **2019**, *31*, e1901796. [CrossRef] [PubMed]
17. Wezendonk, T.A.; Sun, X.; Dugulan, A.I.; van Hoof, A.J.F.; Hensen, E.J.M.; Kapteijn, F.; Gascon, J. Controlled formation of iron carbides and their performance in Fischer-Tropsch synthesis. *J. Catal.* **2018**, *362*, 106–117. [CrossRef]
18. Bukur, D.B.; Lang, X.; Rossin, J.A.; Zimmerman, W.H.; Rosynek, M.P.; Yeh, E.B.; Li, C. Activation studies with a promoted precipitated iron Fischer-Tropsch catalyst. *Ind. Eng. Chem. Res.* **2002**, *28*, 1130–1140. [CrossRef]
19. Bukur, D.B.; Nowicki, L.; Manne, R.K.; Lang, X.S. Activation Studies with a Precipitated Iron Catalyst for Fischer-Tropsch Synthesis. *J. Catal.* **1995**, *155*, 366–375. [CrossRef]
20. Bukur, D.B.; Lang, X.; Ding, Y. Pretreatment effect studies with a precipitated iron Fischer–Tropsch catalyst in a slurry reactor. *Appl. Catal. A Gen.* **1999**, *186*, 255–275. [CrossRef]
21. Lee, Y.H.; Lee, D.-W.; Kim, H.; Choi, H.S.; Lee, K.-Y. Fe–Zn catalysts for the production of high-calorie synthetic natural gas. *Fuel* **2015**, *159*, 259–268. [CrossRef]
22. Ding, M.; Yang, Y.; Li, Y.; Wang, T.; Ma, L.; Wu, C. Impact of H_2/CO ratios on phase and performance of Mn-modified Fe-based Fischer Tropsch synthesis catalyst. *Appl. Energy* **2013**, *112*, 1241–1246. [CrossRef]
23. Bhalothia, D.; Fan, Y.-J.; Huang, T.-H.; Lin, Z.-J.; Yang, Y.-T.; Wang, K.-W.; Chen, T.-Y. Local Structural Disorder Enhances the Oxygen Reduction Reaction Activity of Carbon-Supported Low Pt Loading CoPt Nanocatalysts. *J. Phys. Chem. C* **2019**, *123*, 19013–19021. [CrossRef]
24. Tang, L.; He, L.; Wang, Y.; Chen, B.; Xu, W.; Duan, X.; Lu, A.-H. Selective fabrication of χ-Fe_5C_2 by interfering surface reactions as a highly efficient and stable Fischer-Tropsch synthesis catalyst. *Appl. Catal. B Environ.* **2021**, *284*, 119753. [CrossRef]
25. Emiel de Smit, F.C.; Andrew, M.B.; Safonova, O.V.; van Beek, W.; Sautet, P.; Weckhuysen, B.M. Stability and Reactivity of ϵ—χ—θ Iron Carbide Catalyst Phases in Fischer-Tropsch Synthesis: Controlling μ_C. *J. Am. Chem. Soc.* **2010**, *132*, 14928–14941. [CrossRef] [PubMed]
26. Niu, L.; Liu, X.; Liu, J.; Liu, X.; Wen, X.; Yang, Y.; Xu, J.; Li, Y. Tuning carburization behaviors of metallic iron catalysts with potassium promoter and $CO/syngas/C_2H_4/C_2H_2$ gases. *J. Catal.* **2019**, *371*, 333–345. [CrossRef]

27. Zhang, Y.; Cao, C.; Zhang, C.; Zhang, Z.; Liu, X.; Yang, Z.; Zhu, M.; Meng, B.; Xu, J.; Han, Y.-F. The study of structure-performance relationship of iron catalyst during a full life cycle for CO_2 hydrogenation. *J. Catal.* **2019**, *378*, 51–62. [CrossRef]
28. Zhang, Y.; Fu, D.; Liu, X.; Zhang, Z.; Zhang, C.; Shi, B.; Xu, J.; Han, Y.-F. Operando Spectroscopic Study of Dynamic Structure of Iron Oxide Catalysts during CO_2 Hydrogenation. *ChemCatChem* **2018**, *10*, 1272–1276. [CrossRef]
29. Zhu, J.; Wang, P.; Zhang, X.; Zhang, G.; Li, R.; Li, W.; Senftle, T.P.; Liu, W.; Wang, J.; Wang, Y.; et al. Dynamic structural evolution of iron catalysts involving competitive oxidation and carburization during CO_2 hydrogenation. *Sci. Adv.* **2022**, *8*, eabm3629. [CrossRef]
30. Skrypnik, A.S.; Yang, Q.; Matvienko, A.A.; Bychkov, V.Y.; Tulenin, Y.P.; Lund, H.; Petrov, S.A.; Kraehnert, R.; Arinchtein, A.; Weiss, J.; et al. Understanding reaction-induced restructuring of well-defined FexOyCz compositions and its effect on CO_2 hydrogenation. *Appl. Catal. B Environ.* **2021**, *291*, 120121. [CrossRef]
31. Zhang, C.; Xu, M.; Yang, Z.; Zhu, M.; Gao, J.; Han, Y.-F. Uncovering the electronic effects of zinc on the structure of Fe_5C_2-ZnO catalysts for CO_2 hydrogenation to linear α-olefins. *Appl. Catal. B Environ.* **2021**, *295*, 120287. [CrossRef]
32. Xu, Y.; Li, X.; Gao, J.; Wang, J.; Ma, G.; Wen, X.; Yang, Y.; Li, Y.; Ding, M. A hydrophobic FeMn@Si catalyst increases olefins from syngas by suppressing C1 by-products. *Science* **2021**, *371*, 610–613. [CrossRef] [PubMed]
33. Liu, J.; Zhang, A.; Jiang, X.; Liu, M.; Sun, Y.; Song, C.; Guo, X. Selective CO_2 Hydrogenation to Hydrocarbons on Cu-Promoted Fe-Based Catalysts: Dependence on Cu–Fe Interaction. *ACS Sustain. Chem. Eng.* **2018**, *6*, 10182–10190. [CrossRef]
34. Zhang, C.; Cao, C.; Zhang, Y.; Liu, X.; Xu, J.; Zhu, M.; Tu, W.; Han, Y.-F. Unraveling the Role of Zinc on Bimetallic Fe_5C_2–ZnO Catalysts for Highly Selective Carbon Dioxide Hydrogenation to High Carbon α-Olefins. *ACS Catal.* **2021**, *11*, 2121–2133. [CrossRef]
35. Paalanen, P.P.; van Vreeswijk, S.H.; Weckhuysen, B.M. Combined In Situ X-ray Powder Diffractometry/Raman Spectroscopy of Iron Carbide and Carbon Species Evolution in Fe(−Na–S)/α-Al_2O_3 Catalysts during Fischer–Tropsch Synthesis. *ACS Catal.* **2020**, *10*, 9837–9855. [CrossRef]
36. Zhang, Z.; Zhang, J.; Wang, X.; Si, R.; Xu, J.; Han, Y.-F. Promotional effects of multiwalled carbon nanotubes on iron catalysts for Fischer-Tropsch to olefins. *J. Catal.* **2018**, *365*, 71–85. [CrossRef]
37. Lu, J.; Yang, L.; Xu, B.; Wu, Q.; Zhang, D.; Yuan, S.; Zhai, Y.; Wang, X.; Fan, Y.; Hu, Z. Promotion Effects of Nitrogen Doping into Carbon Nanotubes on Supported Iron Fischer–Tropsch Catalysts for Lower Olefins. *ACS Catal.* **2014**, *4*, 613–621. [CrossRef]
38. Teng, X.; Huang, S.; Wang, J.; Wang, H.; Zhao, Q.; Yuan, Y.; Ma, X. Fabrication of Fe_2C Embedded in Hollow Carbon Spheres: A High-Performance and Stable Catalyst for Fischer-Tropsch Synthesis. *ChemCatChem* **2018**, *10*, 3883–3891. [CrossRef]
39. Yang, C.; Zhao, H.; Hou, Y.; Ma, D. Fe_5C_2 nanoparticles: A facile bromide-induced synthesis and as an active phase for Fischer-Tropsch synthesis. *J. Am. Chem. Soc.* **2012**, *134*, 15814–15821. [CrossRef]
40. Li, Y.; Li, Z.; Ahsen, A.; Lammich, L.; Mannie, G.J.A.; Niemantsverdriet, J.W.H.; Lauritsen, J.V. Atomically Defined Iron Carbide Surface for Fischer–Tropsch Synthesis Catalysis. *ACS Catal.* **2018**, *9*, 1264–1273. [CrossRef]
41. Xu, Y.; Zhai, P.; Deng, Y.; Xie, J.; Liu, X.; Wang, S.; Ma, D. Highly Selective Olefin Production from CO_2 Hydrogenation on Iron Catalysts: A Subtle Synergy between Manganese and Sodium Additives. *Angew. Chem. Int. Ed. Engl.* **2020**, *59*, 21736–21744. [CrossRef] [PubMed]
42. Ding, M.; Yang, Y.; Wu, B.; Li, Y.; Wang, T.; Ma, L. Study on reduction and carburization behaviors of iron phases for iron-based Fischer–Tropsch synthesis catalyst. *Appl. Energy* **2015**, *160*, 982–989. [CrossRef]
43. Sun, X.; Liu, X.; Liu, J.; He, Y.; Yin, J.; Song, C.; Lv, Z.; Bai, Y.; Li, Y.-W.; Yang, Y.; et al. Elucidation of The Influence of Cu Promoter on Carburization Prior to Iron-Based Fischer-Tropsch Synthesis: An In Situ X-ray Diffraction Study. *ChemCatChem* **2019**, *11*, 715–723. [CrossRef]
44. Li, S.; Meitzner, G.D.; Iglesia, E. Structure and Site Evolution of Iron Oxide Catalyst Precursors during the Fischer-Tropsch Synthesis. *J. Phys. Chem. B* **2001**, *105*, 5743–5750. [CrossRef]
45. Yamashita, T.; Hayes, P. Analysis of XPS spectra of Fe^{2+} and Fe^{3+} ions in oxide materials. *Appl. Surf. Sci.* **2008**, *254*, 2441–2449. [CrossRef]
46. Tan, P. Active phase, catalytic activity, and induction period of Fe/zeolite material in nonoxidative aromatization of methane. *J. Catal.* **2016**, *338*, 21–29. [CrossRef]
47. Nielsen, M.R.; Moss, A.B.; Bjørnlund, A.S.; Liu, X.; Knop-Gericke, A.; Klyushin, A.Y.; Grunwaldt, J.-D.; Sheppard, T.L.; Doronkin, D.E.; Zimina, A.; et al. Reduction and carburization of iron oxides for Fischer–Tropsch synthesis. *J. Energy Chem.* **2020**, *51*, 48–61. [CrossRef]
48. McNab, A.I.; McCue, A.J.; Dionisi, D.; Anderson, J.A. Quantification and qualification by in-situ FTIR of species formed on supported-cobalt catalysts during the Fischer-Tropsch reaction. *J. Catal.* **2017**, *353*, 286–294. [CrossRef]
49. McCue, A.J.; Mutch, G.A.; McNab, A.I.; Campbell, S.; Anderson, J.A. Quantitative determination of surface species and adsorption sites using Infrared spectroscopy. *Catal. Today* **2016**, *259*, 19–26. [CrossRef]
50. Weiß, J.; Yang, Q.; Bentrup, U.; Kondratenko, E.V.; Brückner, A.; Kubis, C. Operando DRIFT and In situ Raman Spectroscopic Studies on Aspects of CO_2 Fischer-Tropsch Synthesis Catalyzed by Bulk Iron Oxide-Based Catalysts. *ChemCatChem* **2022**, *14*, e202200577. [CrossRef]
51. Ge, X.; Dou, M.; Cao, Y.; Liu, X.; Yuwen, Q.; Zhang, J.; Qian, G.; Gong, X.; Zhou, X.; Chen, L.; et al. Mechanism driven design of trimer Ni_1Sb_2 site delivering superior hydrogenation selectivity to ethylene. *Nat. Commun.* **2022**, *13*, 5534. [CrossRef] [PubMed]

52. Moon, J.; Cheng, Y.; Daemen, L.L.; Li, M.; Polo-Garzon, F.; Ramirez-Cuesta, A.J.; Wu, Z. Discriminating the Role of Surface Hydride and Hydroxyl for Acetylene Semihydrogenation over Ceria through In Situ Neutron and Infrared Spectroscopy. *ACS Catal.* **2020**, *10*, 5278–5287. [CrossRef]
53. Khan, M.K.; Butolia, P.; Jo, H.; Irshad, M.; Han, D.; Nam, K.-W.; Kim, J. Selective Conversion of Carbon Dioxide into Liquid Hydrocarbons and Long-Chain α-Olefins over Fe-Amorphous AlO_x Bifunctional Catalysts. *ACS Catal.* **2020**, *10*, 10325–10338. [CrossRef]
54. Lee, Y.H.; Lee, K.-Y. Effect of surface composition of Fe catalyst on the activity for the production of high-calorie synthetic natural gas (SNG). *Korean J. Chem. Eng.* **2016**, *34*, 320–327. [CrossRef]
55. Chai, J.; Pestman, R.; Chen, W.; Dugulan, A.I.; Feng, B.; Men, Z.; Wang, P.; Hensen, E.J.M. The role of H_2 in Fe carburization by CO in Fischer-Tropsch catalysts. *J. Catal.* **2021**, *400*, 93–102. [CrossRef]
56. Xiang, M.; Zou, J.; Li, Q.; She, X. Catalytic performance of iron carbide for carbon monoxide hydrogenation. *J. Nat. Gas Chem.* **2010**, *19*, 468–470. [CrossRef]
57. Liu, Y.; Chen, J.-F.; Bao, J.; Zhang, Y. Manganese-Modified Fe_3O_4 Microsphere Catalyst with Effective Active Phase of Forming Light Olefins from Syngas. *ACS Catal.* **2015**, *5*, 3905–3909. [CrossRef]
58. Liu, Y.; Lu, F.; Tang, Y.; Liu, M.; Tao, F.F.; Zhang, Y. Effects of initial crystal structure of Fe_2O_3 and Mn promoter on effective active phase for syngas to light olefins. *Appl. Catal. B Environ.* **2020**, *261*, 118219. [CrossRef]
59. Shroff, M.D.; Datye, A.K. The importance of passivation in the study of iron Fischer-Tropsch catalysts. *Catal. Lett.* **1996**, *37*, 101–106. [CrossRef]